

## PAPER

[View Article Online](#)  
[View Journal](#) | [View Issue](#)Cite this: *J. Mater. Chem. A*, 2020, **8**, 9218**Dendrite-free and air-stable lithium metal batteries enabled by electroless plating with aluminum fluoride†**Zaisheng Wang,<sup>‡a</sup> Zhenming Xu,<sup>‡d</sup> Xiaojing Jin,<sup>\*af</sup> Jianhui Li,<sup>c</sup> Qingshuai Xu,<sup>a</sup> Yanan Chong,<sup>a</sup> Changchun Ye,<sup>id a</sup> Weishan Li,<sup>id c</sup> Daiqi Ye,<sup>a</sup> Yingying Lu<sup>id e</sup> and Yongcai Qiu<sup>id \*ab</sup>

Lithium metal, as an ideal anode material for rechargeable and high energy density batteries, suffers from the inherent limitation of sensitivity to dendrite growth and a humid atmosphere. Here, a bifunctional composite interphase is designed to settle these issues. The interphase which is generated on the surface of Li foil through electroless plating with a solution of aluminum fluoride can guide uniform Li plating/stripping behaviors with reduced overpotential and simultaneously improve moisture resistance. Owing to the unique features, the assembled cells with the protected anode and a LiFePO<sub>4</sub> cathode exhibit long cycle life (>300 cycles) with an extraordinary capacity retention (>95%). Further, even if the protected anodes are exposed to humid air (25% relative humidity) for over 24 h, the cells still achieve outstanding performance, comparable to that without exposure. This work thus provides a promising approach towards dendrite-free and air-stable lithium metal batteries.

Received 2nd March 2020

Accepted 17th April 2020

DOI: 10.1039/d0ta02410d

[rsc.li/materials-a](http://rsc.li/materials-a)**Introduction**

High energy and safe chemical storage systems play critical roles in various kinds of emerging fields of technology, where high energy density is the requirement for performance and large-scale applications. Lithium ion batteries (LIBs) with superior energy density, outstanding lifespan and minimal memory effects are widely used in electronic devices, electric vehicles, and grid-scale energy storage.<sup>1–5</sup> However, graphite, as the mostly used commercial anode material, offers a relatively low theoretical capacity of 372 mA h g<sup>−1</sup>, limiting the energy density of LIBs. Therefore, alternative energy storage strategies need to be developed to satisfy the emerging requirements.<sup>6,7</sup>

The Li metal anode with an extraordinary specific capacity (3860 mA h g<sup>−1</sup>) and the lowest electrochemical deposition potential (−3.04 V vs. the standard hydrogen electrode) is regarded as the most promising anode for next generation energy storage systems.<sup>8,9</sup> Nevertheless, the Li metal battery in practical application is still hindered by formidable challenges. Specifically, the uneven electrodeposition of lithium during the repeated charge and discharge processes leads to the formation of dendritic structures, which can bridge the inter-electrode space and thereby produce internal short circuit in cells. Moreover, the volatile lithium metal anode can react with the active electrode and electrolyte, causing severe capacity decay.<sup>10–12</sup> Additionally, the use of Li is also challenging because of its demanding processing requirements. The Li metal anode is corroded immediately on exposure to humid air. Therefore, an air-stable Li metal anode with long-term cycling stability and high coulombic efficiency (CE) is highly desired.

To enable the safe and efficient operation of lithium metal anodes, considerable research efforts have been dedicated to understanding the process of Li metal plating and stripping.<sup>13–15</sup> Nanostructured electrodes,<sup>16,17</sup> protective coatings,<sup>18,19</sup> solid state electrolytes<sup>20,21</sup> and chemical stable interphases<sup>22,23</sup> have significantly suppressed dendrite formation and improved the CE in corrosive carbonate electrolytes up to 98%. Among the various strategies, Li surface protection is a perennial subject of interest due to the spontaneous side reactions between highly reactive Li metal and liquid electrolytes. From the perspective of both their convenience and theory, the protective coating can directly modify the solid electrolyte interface (SEI) layer to alter

<sup>a</sup>Guangdong Provincial Key Laboratory of Atmospheric Environment and Pollution Control, School of Environment and Energy, South China University of Technology, Guangzhou, 510006, China. E-mail: ycqi@scut.edu.cn; jinxj@scut.edu.cn

<sup>b</sup>State Key Laboratory of Luminescent Materials and Devices, South China University of Technology, Guangzhou, China

<sup>c</sup>School of Chemistry and Environment, South China Normal University, Guangzhou 510006, China

<sup>d</sup>Harvard John. A. Paulson School of Engineering and Applied Sciences, Harvard University, 29 Oxford St, Cambridge, Massachusetts, 02138, USA

<sup>e</sup>College of Chemical and Biological Engineering, Zhejiang University, Hangzhou, Zhejiang, China, 310027

<sup>f</sup>Guangdong Provincial Key Lab of Nano-Micro Materials Research, School of Chemical Biology and Biotechnology, Peking University Shenzhen Graduate School, Shenzhen, 518055, China

† Electronic supplementary information (ESI) available. See DOI: 10.1039/d0ta02410d

‡ These authors contributed equally to this work.

Li deposition behavior, impacting the physicochemistries of the ingredient interface. However, the major barrier to the successful implementation of the Li metal anode is the uneven electrodeposition of Li metal in the charge process, leading to locally enhanced Li ion flux and the growth of dendrites.<sup>24–26</sup> In this respect, it is highly desirable to have an effective approach to simultaneously regulate Li deposition by controlling both position and morphology and preventing the undesired side reactions between liquid electrolytes and metallic lithium, further blocking the formation of Li dendrites and enabling high performance LIBs. Herein, we propose a facile and low-cost approach to study Li metal surface stabilization *via* electroless plating of aluminum fluoride directly on the Li metal. Remarkably, we find that consistent with theoretical calculations and expectations, premature cell failure by dendrite growth and proliferation can be essentially eliminated in the plating/stripping processes. Experimental characterization demonstrates that after introducing aluminum fluoride, the ingredient interface is profoundly changed, which can provide superior morphological control and fast surface diffusion of lithium ions. The as-obtained protected Li metal anode enabled dendrite-free and stable cycling over 400 cycles in symmetric cells. When a LiFePO<sub>4</sub> (LFP) cathode was paired with the protected Li metal anode, an extraordinary capacity retention of 95% was achieved after 300 cycles at 1C. Meanwhile, the air stability and electrochemical performances are also significantly improved. Therefore, our work provides a highly effective approach to rationally design a composite interface that overcomes the most serious limitations of spontaneously formed interphases on high capacity metal anodes.

## Results and discussion

The Li plating/stripping behaviors on electrodes of Li foil and the Li foil with a protective layer (named protected Li) are illustrated in Fig. 1. Owing to the uneven deposition of Li ions on the Li foil, the chaotic concentrated Li<sup>+</sup> flux dominates the cyclic process (Fig. 1a). Thus, Li metal fails soon due to it suffering from dendrite growth and severe electrolyte decomposition. For the protected Li foil with the process shown in Fig. 1b, the AlF<sub>3</sub> layer can react with the lithium and generate

LiF and a Li–Al alloy, and the LiF can stabilize the interface and the Li–Al alloy can guide the uniform lithium deposition during cycling. Therefore, the Li<sup>+</sup> distribution and Li surface activity are simultaneously regulated, yielding a uniform and reversible Li stripping/depositing process. Besides, the lithium fluoride can stabilize the interface and mitigate the side reactions between the electrolyte and lithium electrode. Therefore, such a protective layer makes it possible to realize a dendrite-free surface morphology, prolonging the life span of the Li metal anode for deep cycling.

The composite interface is realized *via* direct reduction of aluminum fluoride on Li foil, which is relatively inert and non-reactive with most electrolyte components. The resultant compound reacts with the underlying Li to generate a film which is comprised of the respective lithium-rich LiAl alloy and electronically insulating LiF as a by-product:  $3\text{Li} + \text{AlF}_3 \rightarrow \text{Al} + 3\text{LiF}$ . The aluminum fluoride layer undergoes reactions with the underlying lithium:  $y\text{Li} + z\text{Al} \rightarrow \text{Li}_y\text{Al}_z$  (Fig. S1†). The result is confirmed by the X-ray diffraction (XRD) pattern in Fig. 2a. The presence of Al peaks, Li–Al alloy peaks and Li peaks confirms the Al metal formation by the reaction of AlF<sub>3</sub> with lithium. The peak at 23° is the index of AlF<sub>3</sub> and the peak at 65° is the index of LiF (Fig. S3†). Based on the phase diagram (Fig. S2†), the Li–Al alloy composition should be mainly Al<sub>4</sub>Li<sub>9</sub>, because the lithium is in excess. The schematic of the proposed lithium metal protection technique using the AlF<sub>3</sub> coating layer is shown in Fig. 1b. The Li–Al alloy layer can guide the uniform Li deposition and provide superior morphological control. Fig. 2b and c show the X-ray photoelectron spectra (XPS) for the Li electrode after the chemical reaction. The Al 2p spectra show peaks at 74.5 and 77.2 eV, respectively.<sup>27</sup> In case of the F1 spectra, the peak at 685.1 eV indicates AlF<sub>3</sub>, while that at 688.1–689.2 eV with a shift in the energy indicates LiF as shown in the spectra before cycling.<sup>28</sup> The peak position analysis demonstrates that the AlF<sub>3</sub> film consists of two chemical compositions rather than a physical mixture of LiF or AlF<sub>3</sub>. Fig. 2d and g show the AlF<sub>3</sub> protected Li surface structure using scanning electron microscopy (SEM). Two different layers can be clearly observed from the typical cross-sectional SEM image, in agreement with the above results. The chemical composition of the layers was mapped using energy dispersive X-ray spectroscopy (EDX) as shown in Fig. 2e, f, h, i. It is clearly seen that the Al and F elements are evenly plated on the Li surface. The results suggest that an artificial solid electrolyte interphase composed of LiF, Al, and the Li–Al alloy is homogeneously formed on the Li foil.

In order to evaluate the energetic landscapes at the electrode–electrolyte interphases, we performed density-functional theory (DFT) calculations for the activation energy barrier of lithium diffusion. AlF<sub>3</sub> can be reduced by Li to form LiF, Al metal and even Li–Al binary alloys. According to the DFT calculated phase diagram of the Li–Al binary system (Fig. 3a), the reduction product of Al metal with abundant Li is Li<sub>9</sub>Al<sub>4</sub> with a formation energy of −0.153 eV per atom. Therefore, the effective protective layer is a mixture of LiF, Al and Li<sub>9</sub>Al<sub>4</sub>. We performed CI-NEB calculations to study lithium atom diffusion on the surfaces of the above mentioned protective layer mixture. Based on previous research, the (100) surface of LiF and the

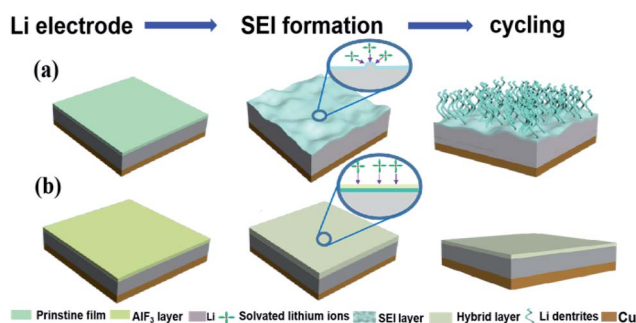


Fig. 1 Schematics of the Li anode structures and the contribution of AlF<sub>3</sub> during SEI formation and cycling. (a) The general Li metal and (b) AlF<sub>3</sub> protected Li metal anodes.

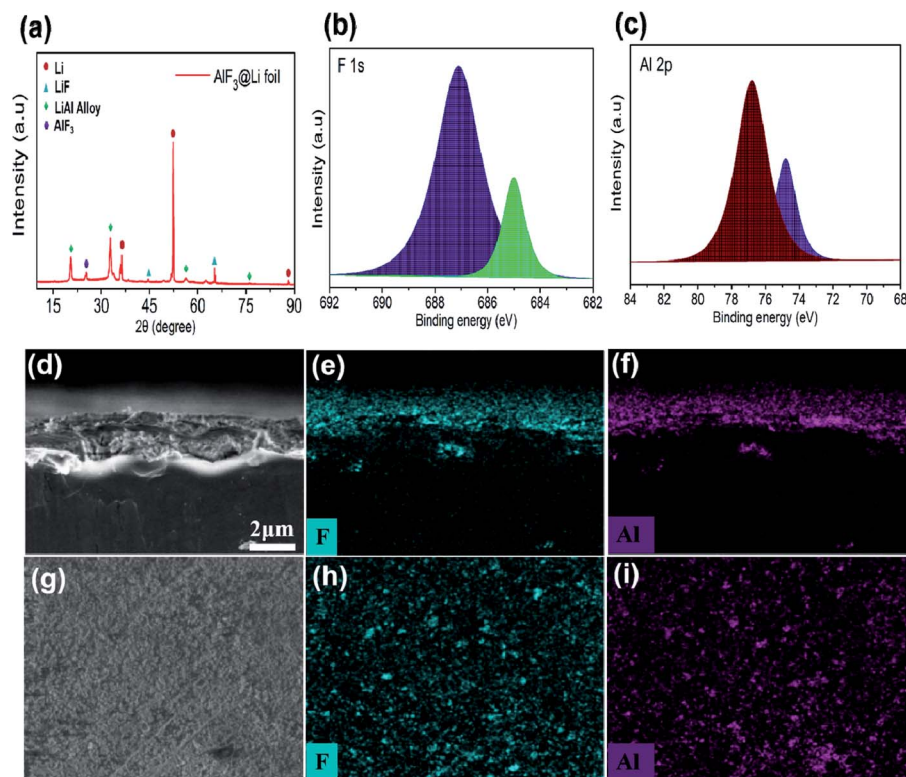


Fig. 2 Surface characterization of the lithium anode  $\text{AlF}_3\text{@Li}$ : (a) XRD pattern of  $\text{AlF}_3\text{@Li}$ . XPS spectra of (b) F 1s and (c) Al 2s. (d) Cross-sectional and (g) top view SEM images and the corresponding elemental distribution of (e, h) F and (f, i) Al.

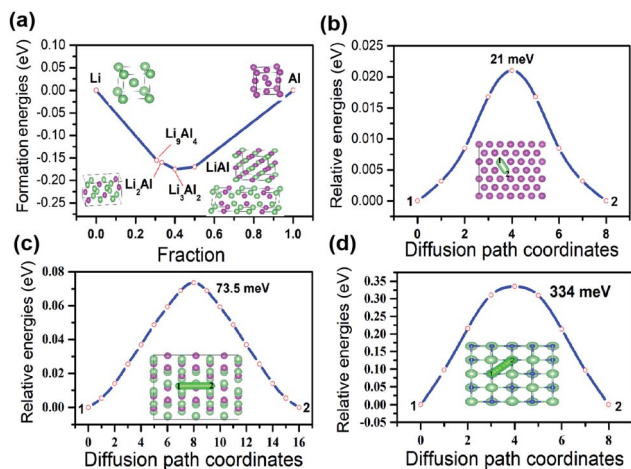


Fig. 3 (a) DFT calculated formation energies of the Li–Al binary alloys; energy variations of Li ion diffusion on (b) Al (111), (c)  $\text{Li}_9\text{Al}_4$  (100) and (d) LiF (100) surfaces, respectively.

(111) close-packed hexagonal surface of Al was chosen for CI-NEB calculations as the most stable facets in their crystal phase. For the  $\text{Li}_9\text{Al}_4$  alloy, (100) was selected with the lowest surface energy according to our calculation, as listed in Table S1.† The CI-NEB calculated results indicate that Li atom diffusion between two adjacent hollow adsorption sites on the Al (111) surface is very fast with an extremely small activation energy barrier of 21 meV (Fig. 3b), less than  $k\text{BT} \sim 26$  meV at

room temperature. The activation energy barrier of Li atom diffusion on the  $\text{Li}_9\text{Al}_4$  (100) surface is calculated to be 73 meV (Fig. 3c), which is also comparable to that on the Al (111) surface and shows excellent surface Li ion diffusion ability. Li diffusion on the LiF (100) surface has a relatively high activation energy barrier of 334 meV (Fig. 3d), and also occurs along a path connected to two adjacent stable adsorption sites on top of F atoms. However, the energy barrier of Li ion diffusion on the LiF (100) surface is comparable to those of oxide-type solid-state electrolyte materials, showing the relatively fast Li ion diffusion on the LiF (100) surface. In summary, the CI-NEB calculations reveal excellent Li diffusion ability on the surfaces of coating layer mixtures, which is quite beneficial for uniform Li deposition and effectively prevents the formation of Li dendrites.

The cycling capability of galvanostatic symmetric cells was compared between Li foil and protected Li. Fig. S4† shows the voltage profiles of the symmetric cells during the 1st, 10th, 50th, and 100th cycles, with the current density fixed at  $1 \text{ mA cm}^{-2}$  and capacity fixed at  $1 \text{ mA h cm}^{-2}$  in carbonate-based electrolytes. For the Li foil symmetric cell, high overpotential could be seen at the beginning of the charge process during the first cycle, owing to the preserved poor ionic conductivity of the SEI on the Li surface and the formation of an insulating SEI by continuous reactions between Li and the electrolyte, which hinder ion transport at the interface. Additionally, high overpotential could also be seen at the beginning and end of the discharge process, corresponding to the increased difficulty of



Li nucleation beneath the thick SEI and the usage of previously unused fresh Li beneath the surface, respectively. This effect faded with the cycle number because of the side reactions between the electrolyte and Li electrode, growth of Li dendrites due to non-uniform Li deposition after plating/stripping, and formation of a fragile/unstable SEI.<sup>29</sup> Eventually, the overpotential increases and causes premature death of the cell. In contrast, the protected Li showed a low overpotential below 50 mV during the charge and discharge processes, as well as better stability when proceeding with cycling. The hybrid artificial SEI, formed by treatment with  $\text{AlF}_3$ , physically protects the Li from side reactions with the electrolyte and provides a route for uniform Li deposition. The SEI components such as Al can reversibly store Li by alloying. The presence of a Li-Al alloy in the protective SEI layer facilitates uniform Li diffusion to reversibly store Li by plating on the Li electrode underneath the SEI.<sup>30</sup> This superiority can be further proven in Fig. 4a, where the symmetric cells using the protected Li offered a consistent, stable low overpotential of about 50 mV during the first 100 cycles, much lower than that of the Li foil counterparts, whose overpotential fluctuated between 100 and 200 mV and a marked overpotential increase could be seen after 100 hours. The results were further verified by electrochemical impedance spectroscopy (EIS), which showed clear consistence of internal impedance evolution (Fig. S5 and S6†). For the cell based on Li foil, in the initial state, the charge transfer impedance (the semicircle) was 83.2  $\Omega$ , indicating that the native surface of Li metal is highly resistive. With the cycle proceeding to 100 h and 200 h, the charge transfer impedance increased to 99.4 and 196.0  $\Omega$ , respectively, which was consistent with the large polarization observed in Fig. 4a for the Li foil-based cells. The increasing impedance is mainly due to the sustained consumption of the electrolyte in side reactions. In contrast, a small and stable

charge transfer impedance of 60.5  $\Omega$  was still maintained by the cell using the protected Li. After 800 h of cycling, the charge transfer impedance slightly increased to 78.8  $\Omega$ , indicating fast charge transfer through such a highly stable interface. Afterwards, cycling tests were carried out under increased current densities of 3  $\text{mA cm}^{-2}$  (Fig. 4b) and 5  $\text{mA cm}^{-2}$  (Fig. 4c) with the capacity fixed at 1  $\text{mA h cm}^{-2}$ . The difference in cycling stability became more distinct with the increase of the current density. The overpotential of the protected Li increased from 75 mV at 3  $\text{mA cm}^{-2}$  to 120 mV at 5  $\text{mA cm}^{-2}$ . Meanwhile, stable and smooth cycling plateaus were maintained over 300 h and 50 h. In contrast, the Li foil showed not only a much higher overpotential but also marked fluctuation during the charge and discharge processes and the cycling stability decayed after 50 h and 25 h at 3 and 5  $\text{mA cm}^{-2}$ , respectively. In Fig. S7,† the voltage profile comparison was revealed between Li foil and protected Li. Symmetric cell cycling was carried out under various areal capacity from 1 to 5  $\text{mA h cm}^{-2}$  and was finally turned back to 1  $\text{mA h cm}^{-2}$ , and the areal capacity of a commercial battery was about 3  $\text{mA h cm}^{-2}$ . Continuous flat charging and discharging plateaus with an obvious lower overpotential can be seen at all applied areal capacities for the protected Li, manifesting its potential for commercial level cycle capability.

CE is an important index that determines the lifespan of a lithium metal anode in practical batteries, in which the lithium metal source is commonly limited. The CE has a necessarily close connection with the SEI layer. A well protected layer can prevent the direct chemical reactions between Li and the electrolyte well, leading to a high CE and a long life in a working battery. The utilization of Li during repeated plating and stripping processes is numerically indicated by the CE of Li|Cu half cells. The average CE of a cell with protected Li reaches 97.2% at a current density of 1.0  $\text{mA cm}^{-2}$ , which is much higher than that of Li foil at 87.5% (Fig. S8†). It's clearly shown that the protected Li enables stable SEI formation and flat electrodeposition and thereby effectively improves the CE.

It is hypothesized that macroscopic morphological evolution during electrodeposition is dependent on the interfacial ion mobility and the initial nucleation process. We performed direct visualization experiments using an optical microscope to monitor the deposition behavior of Li in Li/Li symmetrical cells. Specifically, an in-house structure with a visualization setup was used (Fig. S9†). Two pieces of Li foils were used as electrodes and the center tube was filled with the electrolyte. At a current density of 10  $\text{mA cm}^{-2}$ , morphological changes of the electrode were recorded at equal time intervals up to 10 min (2  $\text{mA h cm}^{-2}$ ), as shown in Fig. 5a. The Li foil generated mossy Li at the beginning and numerous dendrites continuously emerged on Li foil within the following 10 min (Video S1†). In contrast, no dendrites can be observed on the lithium surface with the protected Li after the same amount of time (Video S2†). Furthermore, in comparison to the electrodeposited protected Li, the Li deposited on the Li foil was darker in color, indicative of instantaneous side reactions because of an unstable SEI.<sup>24</sup> A quantitative comparison of the morphological changes was obtained by plotting the height of the deposit at different times

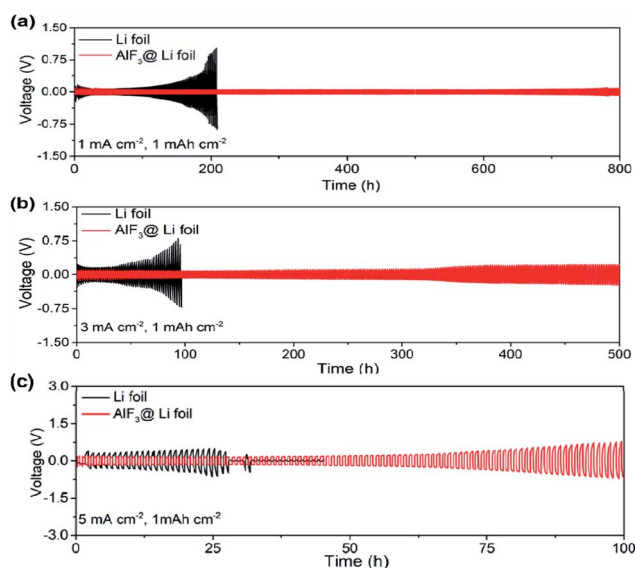


Fig. 4 Electrochemical characterization of the  $\text{AlF}_3$  protected anode. A comparison of the cycling stability of the symmetric  $\text{AlF}_3$  protected Li anode and Li foil anode cells at a current density of (a) 1.0  $\text{mA cm}^{-2}$ , (b) 3.0  $\text{mA cm}^{-2}$ , and (c) 5.0  $\text{mA cm}^{-2}$ , respectively.

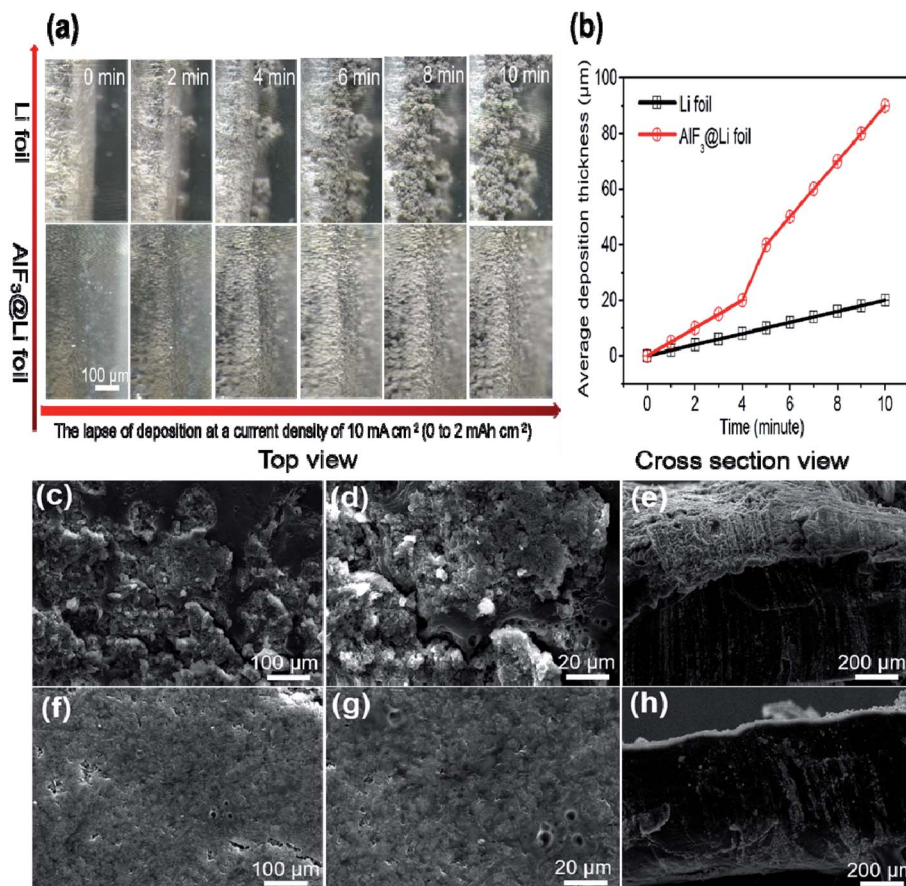


Fig. 5 *In situ* investigation of Li-ion plating behavior by operando optical microscopy. (a) Li deposited with Li foil and AlF<sub>3</sub>@Li foil during continuous plating on the Li metal electrodes at a current density of 10 mA cm<sup>-2</sup>. (b) Average deposition thickness as a function of time for Li foil and AlF<sub>3</sub>@Li foil, obtained by visualization experiments. Top-view (c, d, f, g) and cross-sectional (e, h) SEM images of the Li foil (c, d, e) and AlF<sub>3</sub>@Li foil (f, g, h) electrodes after 200 cycles. The cycling current density was fixed at 1 mA cm<sup>-2</sup> and the stripping/plating capacity was 1 mA h cm<sup>-2</sup>.

as shown in Fig. 5b. Using a linear fit, the growth rate of Li deposition was calculated to be 12.5 nm s<sup>-1</sup>. Thus, it is evident that the protected Li results in improved long-term electrodeposition stability. The deposition conditions with different cycling capacities were also analyzed as shown in Fig. S10.† With fixed capacities of 0.1 mA h cm<sup>-2</sup> (Fig. S10a and d†), 0.5 mA h cm<sup>-2</sup> (Fig. S10b and e†) and 1 mA h cm<sup>-2</sup> (Fig. S10c and f†), the deposition morphology still remained oblate and dendrite-free. In particular, when the cycling capacity was set at 1 mA h cm<sup>-2</sup>, the protected Li metal tended to deposit as scales as shown in Fig. S10c.† Based on this evidence, we can conclude that under the influence of the protective layer, the Li diffusion path is homogeneous and Li deposits from the bottom gaps to the top of the LiAl alloy host, resulting in the surface of the Li anode being covered by lithium scales.

To observe the morphology variation of Li foil and protected Li in symmetrical cells after cycling, both top-view and cross-sectional SEM images were recorded after 200 cycles at 1 mA cm<sup>-2</sup> with a stripping/plating capacity of 1 mA h cm<sup>-2</sup>. For comparison, Fig. S11a–c† show the relatively smooth surface and cross-sectional image of the bare Li foil before cycling. After 200 cycles of Li stripping and plating at a current density of 1 mA cm<sup>-2</sup> and a capacity of 1 mA h cm<sup>-2</sup>, the Li foil surface was

covered with numerous dendrites, tangled with each other (Fig. 5c and d). Additionally, a thick side reaction SEI film can be obviously seen in the cross-sectional view (Fig. 5e). However, for the protected Li, the smooth surface was maintained because of the confining effect and the homogeneous growth on the surface. No dendrite growth could be observed on the surface (Fig. 5f and g), and the cross-sectional view showed an intact and thinner SEI film (Fig. 5h). The results suggest that the protected Li can effectively enable uniform Li deposition and inhibit the side reactions.

The practical viability of the protective layer on the lithium metal anode was further validated through full cell testing, in which the metallic lithium anode was paired with a LFP cathode with a very high mass loading (10 mg cm<sup>-2</sup> or 1.6 mA h cm<sup>-2</sup>) as shown in Fig. 6. LFP based batteries with Li foil and protected Li presented distinctive specific capacity retention after 300 cycles (Fig. 6a). The discharge capacity of the Li foil cell gradually dropped to 38 mA h g<sup>-1</sup> at the 300th cycle with a capacity retention of 25%, while the protected Li cell still maintained a reversible capacity of about 145 mA h g<sup>-1</sup> under the same conditions, corresponding to a capacity retention of 95%. The superior discharge capacity in long-term cycling demonstrates that the AlF<sub>3</sub> treatment is an effective way to achieve

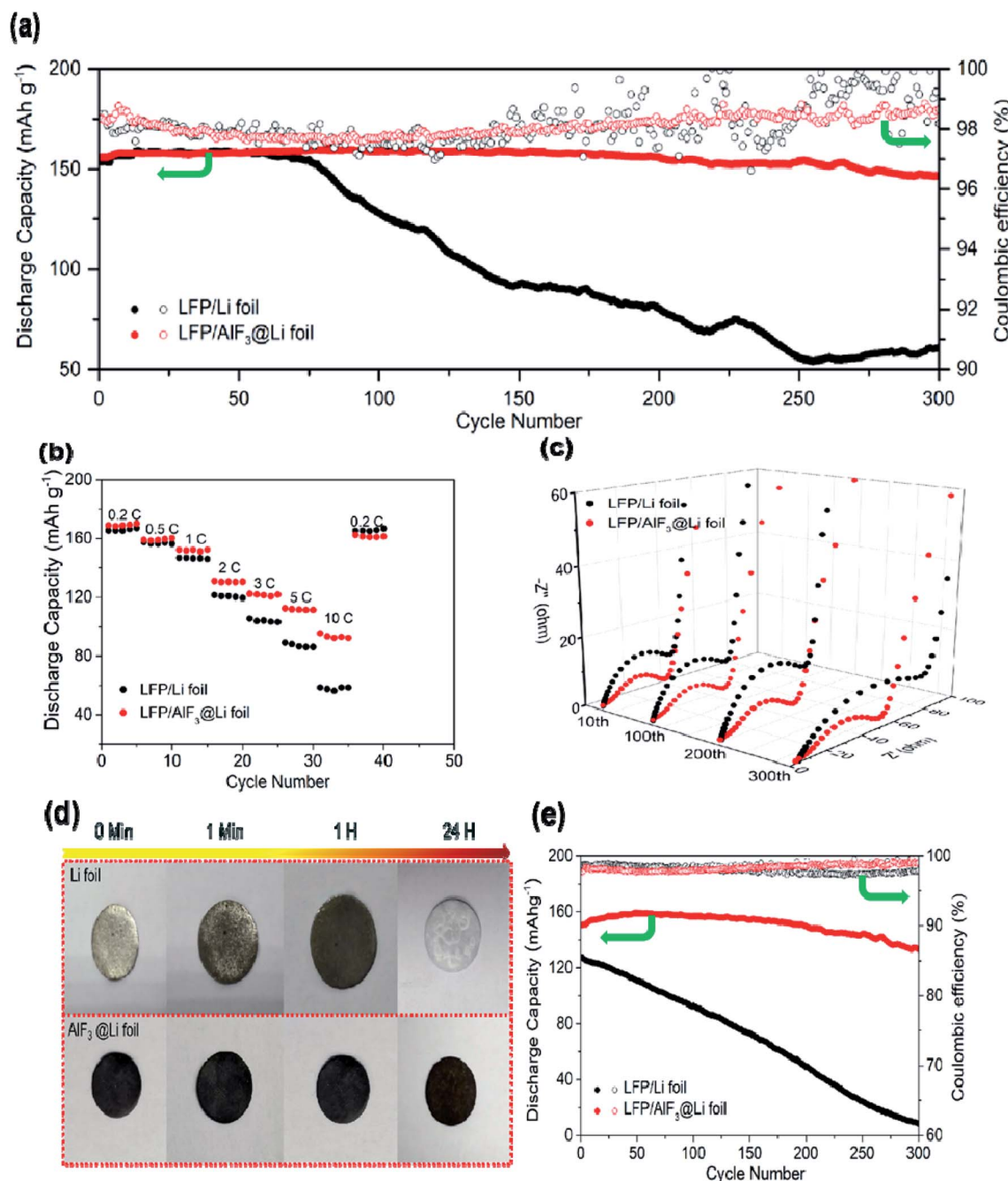


**Fig. 6** Electrochemical performance of rechargeable lithium metal batteries. (a) Galvanostatic cycling performance of Li–LiFePO<sub>4</sub> (LFP) batteries at a 1C rate in the voltage range from 2.8 to 4.0 V. (b) Rate capability of Li–LFP batteries at various rates from 0.2C to 10C. (c) EIS comparison of Li–LFP batteries after 10, 100, 200 and 300 cycles at a 1C rate. (d) Digital images of Li foil and AlF<sub>3</sub> protected Li foil exposed to air at 25 °C and 25% humidity. The diameter of lithium foil is 15.6 mm. (e) Cycling performance of Li–LFP batteries at a 1C rate in the voltage range from 2.8 to 4.0 V using Li foil and AlF<sub>3</sub> protected Li foil after exposure to air at 25 °C and 25% relative humidity for 24 h.

outstanding cell stability. Moreover, the CE of the cell with protected Li is higher than that of the Li foil-based cell. The lower CE in Li foil can be attributed to the side reactions and formation of an unstable and fragile SEI, while the protected Li exhibits a stabilized SEI. This outstanding result was further proved by the voltage–capacity curves and voltage hysteresis. Higher overpotential could be observed for Li foil at the beginning of each charge and discharge plateau, owing to the

sluggish kinetics at the Li foil/electrolyte interface (Fig. S12†). However, with the protected Li, even matched with a LiNi<sub>0.5</sub>Co<sub>0.2</sub>Mn<sub>0.3</sub> (LNCM) cathode, the cell displayed good performance (Fig. S13 and S14†). The superiority was also confirmed by the rate capability. The Li–LFP battery only offered capacities of 165.4 mA h g<sup>-1</sup> at 0.2C, 156.7 mA h g<sup>-1</sup> at 0.5C, 150.2 mA h g<sup>-1</sup> at 1C, 120.7 mA h g<sup>-1</sup> at 2C, 103.4 mA h g<sup>-1</sup> at 3C, 88.2 mA h g<sup>-1</sup> at 5C and 57.6 mA h g<sup>-1</sup> at 10C. In



comparison, using the protected Li, the Li-LFP cell exhibited increasing capacities of  $168.4 \text{ mA h g}^{-1}$  at 0.2C,  $158.8 \text{ mA h g}^{-1}$  at 0.5C,  $152.3 \text{ mA h g}^{-1}$  at 1C,  $130.4 \text{ mA h g}^{-1}$  at 2C,  $121.3 \text{ mA h g}^{-1}$  at 3C,  $111.5 \text{ mA h g}^{-1}$  at 5C and  $93 \text{ mA h g}^{-1}$  at 10C (Fig. 6b). Here, all specific capacities were calculated on the basis of active LFP mass. These results in full cells may be related to the reduced hysteresis using the protected Li. The hybrid has high ionic conductivity, low diffusion energy, and high surface energy, which allow sufficient Li-ion diffusion during plating. However, the poor rate capability using Li foil is attributed to the failure of the conductive framework in the anode induced by the highly resistive, fragile/unstable SEI formed and dead Li covering the Li anode. The merits were further verified by the EIS test. Fig. 6c shows the Nyquist plots of Li-LFP batteries at different cycles. The high-frequency semi-circles are good indicators of the charge transfer resistance on the electrode-electrolyte interfaces. Initially, the interfacial resistance of the Li foil is relatively higher than that of the protected Li. With the increasing cycling number, for the Li foil, the charge transfer resistance rapidly increased. This phenomenon can be attributed to the continuous side reactions because of the exposure of Li to the electrolyte, and the accumulated SEI layer with poor Li-ion conductivity leads to high resistance. However, the cell using protected Li shows a rather stable and consistently low resistance even after 300 cycles (Fig. S15<sup>†</sup>). These results guarantee that the protected Li can be cycled with a lower driving force for charge transfer.

To further verify the regulation of Li metal activity by the protective layer, both the Li foil and protected Li were exposed to air at 25°C and 25% relative humidity. Fig. 6d presents the photos of Li surface evolution after exposure to air. Initially, the Li foil presented a reflection of metallic luster, in contrast to the

matte color of the protected Li. The surface color of the protected Li visually remained unchanged even after exposure to air for 24 h, while the Li foil surface tarnishes immediately after 1 min of exposure to air, due to the formation of lithium based compounds such as nitrides, hydroxides, and carbonates, which were further identified from the XRD results (Fig. S16<sup>†</sup>). These derivatives may generate adverse influence during the cycling process. The optical micrographs confirmed the regulation effect of the Li metal surface activity by the protective layer. In order to confirm the effect of the protective layer on the foil, the electrode was examined using full cells (Fig. 6e). The initial discharge capacity of cells with the protected Li was  $153 \text{ mA h g}^{-1}$  and still remained at  $133 \text{ mA h g}^{-1}$  after 300 cycles at 1C, which maintained almost the same level compared to the control group. By contrast, the capacity of the Li foil cell was only  $125 \text{ mA h g}^{-1}$ , followed by a sharp decrease, and dropped to  $8 \text{ mA h g}^{-1}$  after 300 cycles. Additionally, the CE of the protected Li remained almost above 98.5%, while that of the Li foil gradually declined with the subsequent cycles. As shown in Fig. S17,<sup>†</sup> there was no real distinction of the capacity retention using the protected Li before and after exposure to air for 24 h. The superior electrochemical performance demonstrates the effectiveness of the protected Li.

XPS was used to analyze the chemical compositions of surface films generated on the Li and protected Li metal anode before and after 100 cycles at  $1.0 \text{ mA cm}^{-2}$  (Fig. 7 and S18<sup>†</sup>). The comparison of various atomic ratios of the protected Li and Li foil is shown in Fig. S19.<sup>†</sup> In the C 1s spectra (Fig. 7a and e), the peak situated at 284.7 eV can be attributed to C-C/C-H. The peak at 286.8 eV is assigned to the C-O bond in carbonic ester, and the peak located at 290.4 eV is attributed to C=O in polycarbonates and lithium carbonates.<sup>31</sup> Apparently, the ratio of

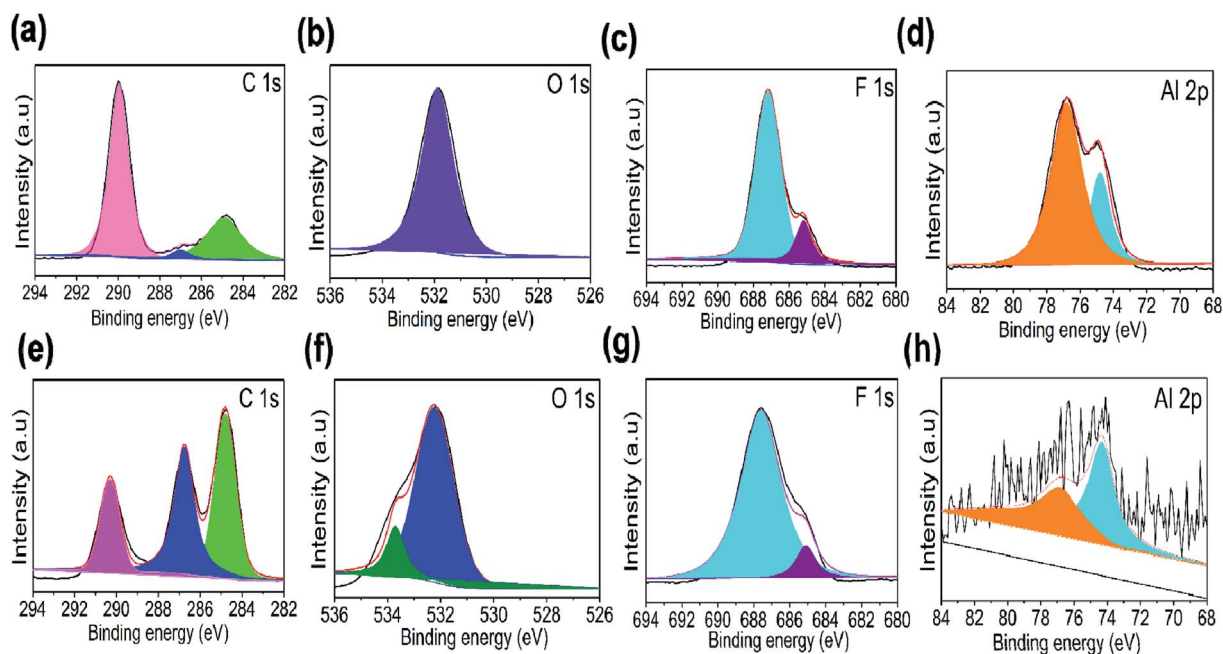


Fig. 7 Surface chemistry of the  $\text{AlF}_3$  protected Li metal anode before (a–d) and after (e–h) 100 cycles. X-ray photoelectron spectroscopy (XPS) results of (a, e) C 1s; (b, f) O 1s; (c, g) F 1s; (d, h) Al 2p.

the C=O bond of protected Li is weaker compared to that of the Li foil (Fig. S18e†), indicating that fewer side reactions of the electrolyte occur on the surface of the protected Li. The side reaction products are mainly derived from electrolyte solvent decomposition.<sup>32</sup> In the O1s spectra (Fig. 7b and f), the peaks situated at 529.0 and 532.2 eV are attributed to lithium alkyl carbonates and  $\text{Li}_2\text{CO}_3$ , respectively.<sup>33,34</sup> In the F 1s spectra (Fig. 7c and g), there are two peaks located at 685.1 and 687.0 eV, corresponding to LiF and  $\text{Li}_x\text{PO}_y\text{F}_z$ ,<sup>25</sup> respectively. It can be seen that the relative intensity of  $\text{Li}_x\text{PO}_y\text{F}_z$  increased after cycling, which can be attributed to more lithium hexafluorophosphate being reduced on the lithium metal anode. In addition, in the Li foil (Fig. S18g†) and  $\text{AlF}_3$  protected Li foil after 100 cycles, the contact of the LiF with Li foil was much stronger than that with the  $\text{AlF}_3$  protected Li electrode, indicating that LiF is the main ingredient in the solid state electrolyte; thus the  $\text{AlF}_3$  protected Li electrode cannot affect the Li ion diffusion energy barrier. The Al 2p spectrum (Fig. 7d and h) can be split into two parts located at 76.8 and 74.2 eV ( $2p^{1/2}$  and  $2p^{3/2}$ ) due to spin-orbit coupling.<sup>35</sup> Both Al 2p peaks become weak after 100 cycles, possibly due to the by-products of electrolyte decomposition and the newly plated Li and Li–Al alloy covering the electrode surface. In the P 2p spectra (Fig. S18d and h†), the peaks at 134.5 and 137.1 eV are characteristic of  $\text{Li}_x\text{PO}_y\text{F}_z$  and  $\text{Li}_x\text{PF}_y$ , and can be attributed to the decomposition of the salt ( $\text{LiPF}_6$ ) in the electrolyte.<sup>32</sup> Specifically, the composite interface constructed by the electroless plating reaction can improve the electrochemical performance of the lithium metal anode, thereby yielding superior cycling stability.

## Conclusion

In this work, a composite solid interface on Li metal is constructed by electroless plating reactions of an aluminum fluoride-based solution and Li metal. The as-obtained Li metal anode can simultaneously guide the uniform deposition of Li metal, avoid the formation of lithium dendrites and mitigate the side reactions between the Li metal anode and electrolyte. Furthermore, the air stability and electrochemical performances are also significantly improved. The new interface enables dendrite-free cycle stability over 800 hours in symmetric cells. When a  $\text{LiFePO}_4$  (LFP) cathode is paired with the protected Li metal anode, an extraordinary capacity retention of 95% is achieved after 300 cycles at 1C. Our finding provides a simple and inexpensive strategy to stabilize lithium metal, which fundamentally changes its electrodeposition behaviour from dendritic to non-dendritic, and opens up a new and promising research direction.

## Experimental section

### Preparation

Battery grade carbonate ester, ethylene carbonate (EC), diethyl carbonate (DEC), ethyl methyl carbonate (EMC) and ethylene glycol dimethyl ether (DME) were provided by Guangzhou Tinci Materials Technology Co., Ltd, China. Aluminum fluoride ( $\text{AlF}_3$ , 99.9%) was purchased from Shanghai Aladdin Bio-Chem

Technology Co., LTD. Lithium hexafluorophosphate ( $\text{LiPF}_6$ ) was bought from Hashimoto Chemical corporation. They were all used without further purification.  $1.0 \text{ mol L}^{-1}$   $\text{LiPF}_6$  in EC/DEC/EMC (3 : 2 : 5, by weight) was used as the electrolyte. Electrolyte preparation was performed in a pure argon-filled glove box (Vigor, China), and the oxygen and water contents were controlled to less than 0.1 ppm. The preparation of protected Li was as follows: the Li foil was polished with abrasive paper and then immersed into a supersaturated solution of  $\text{AlF}_3$  in a carbonate ester electrolyte for over 48 h for sufficient reaction, and after that the as-prepared protected Li was washed with anhydrous DEC thrice to remove the residual impurities.

### Computational methods

All calculations were carried out by using the projector augmented wave method in the framework of density functional theory (DFT),<sup>36</sup> as implemented in the Vienna *ab initio* Simulation Package (VASP). The generalized gradient approximation (GGA) and Perdew–Burke–Ernzerhof (PBE) exchange functional<sup>37</sup> was used. Structural relaxation calculations were performed by using the spin-polarized GGA method.<sup>37</sup> The plane-wave energy cutoff was set to 500 eV, and the Monkhorst–Pack method<sup>38</sup> with  $7 \times 7 \times 7$ ,  $2 \times 7 \times 6$  and  $5 \times 5 \times 5$  was employed for the Brillouin zone sampling of Al,  $\text{Li}_9\text{Al}_4$  and LiF bulks, respectively. In addition, the Al and  $\text{Li}_9\text{Al}_4$  slab super cell calculations used the same k-point mesh densities of the *ab*-plane direction as Al,  $\text{Li}_9\text{Al}_4$  and LiF bulks. The convergence criteria were set to  $10^{-5}$  eV per atom and  $0.01 \text{ eV \AA}^{-1}$ , respectively. A vacuum of  $15 \text{ \AA}$  was included to isolate the slabs for reducing the interactions between each slab. Activation energy barriers of lithium atom diffusion were calculated by using the climbing image nudged elastic band (CI-NEB) method<sup>39</sup> based on the super cell model, which has been successfully applied for research on alkali metal ion diffusion in battery materials.<sup>40,41</sup>

### Electrochemical testing

Electrochemical studies were performed in 2025 coin cells. For the impedance and lithium plating/stripping studies, symmetric cells (fresh lithium on each side or protected lithium foil on each side) were assembled with  $40 \mu\text{L}$  of  $1.0 \text{ mol L}^{-1}$   $\text{LiPF}_6$  in EC/DEC/EMC (3 : 2 : 5, by weight) as the electrolyte. We used a protocol of 1 h of stripping followed by 1 h of plating with a current density of  $1 \text{ mA cm}^{-2}$ . To investigate the performance of the protective layer compared to the lithium metal anode, cells were fabricated with  $\text{LiNi}_{0.5}\text{Co}_{0.2}\text{Mn}_{0.3}$  (LNCM) or  $\text{LiFePO}_4$  (LFP) as the cathode. LNCM and LFP cathodes were fabricated by coating a mixture of 90 wt% LNCM and LFP (Hunan Shanshan Advanced Materials Co. Ltd, China), 10 wt% Super-P and 10 wt% polyvinylidene fluoride (PVDF) binder on aluminum foil. The cathodes were cut into disks with a diameter of 14 mm and dried at  $60^\circ\text{C}$  prior to use. The areal loading of LNCM was about  $10 \text{ mg cm}^{-2}$ . Approximately  $70 \mu\text{L}$  of  $1.0 \text{ mol L}^{-1}$   $\text{LiPF}_6$  in EC/DEC/EMC (3 : 2 : 5, by weight) was used as the electrolyte. The asymmetric Li– $\text{LiFePO}_4$  and Li– $\text{LiNi}_{0.5}\text{Co}_{0.2}\text{Mn}_{0.3}$  batteries were cycled in a voltage range of 2.8–4.0 V and 3.0–4.3 V (vs. Li/Li<sup>+</sup>) in carbonate based electrolytes, respectively.



Electrochemical impedance spectroscopy (EIS) was performed using a PGSTAT-30 electrochemical workstation (Metrohm, Netherlands). The frequency range and potential amplitude of the PGSTAT-30 electrochemical workstation were set to  $10^5$ –0.1 Hz and 5 mV, respectively. Optical microscopy experiments were carried out using a home-made optical cell. Cu foil was employed as the current collector and Li electrodes were placed on each side of a slot separated by  $1.0 \text{ mol L}^{-1} \text{ LiPF}_6$  in EC/DEC/EMC (3 : 2 : 5, by weight) as the electrolyte. The optical cell was assembled with a fluorine rubber ring. All operations were conducted in an Ar-filled glove box with a water and oxygen content below 0.1 ppm. An optical microscope combined with a CCD camera can record the real-time morphology evolution through a transparent quartz window during the operation of Li metal electrodes at a current density of  $1.0 \text{ mA cm}^{-2}$  and a capacity of  $0.5 \text{ mA h cm}^{-2}$ . For Li||Cu cells, the average Li CEs were determined using a modified method proposed by Zhang *et al.*<sup>42</sup> Briefly, a Li layer of  $1 \text{ mA h cm}^{-2}$  was deposited at  $1 \text{ mA cm}^{-2}$  on the Cu working electrode, then stripping of the Li from the Cu electrode was performed at 1 V versus Li/Li<sup>+</sup>. The average CE was calculated after 100 cycles.

### Characterization

For the purpose of minimizing the contamination of the cycled electrodes for physical characterization, the cycled Lithium metal anodes were washed with anhydrous DMC thrice to remove the LiPF<sub>6</sub> salt and remnant carbonate ester precipitated on the electrode surface after dismantling in a glove box filled with Ar gas. The crystal texture was identified by XRD (Bruker D8 Advance, China) in the  $2\theta$  range of 10–90°. Surface composition was detected by X-ray photoelectron spectroscopy (XPS, ESCALAB 250, USA). For the XPS test, cycled lithium metal anodes were carefully handled to avoid exposure to air. The features of the electrode were monitored using a scanning electron microscope (SEM, JSM-650, Germany).

### Author contributions

Z. Wang, X. Jin and Y. Qiu conceived the idea. Z. Xu performed the related calculations. J. Li, Q. Xu, Y. Chong, C. Ye, W. Li, D. Ye and Y. Lu prepared or provided the materials and testing equipment. Z. Wang, X. Jin and Y. Qiu co-wrote the paper. All the authors discussed the results and commented on the manuscript.

### Conflicts of interest

There are no conflicts to declare.

### Acknowledgements

This work was supported by the National Key Research and Development Program of China (2018YFA0209600) and the Guangdong Science and Technology Program (2017B030314002).

### References

- 1 J. M. Tarascon and M. Armand, *Nature*, 2001, **414**, 359.
- 2 B. Dunn, H. Kamath and J. M. Tarascon, *Science*, 2011, **334**, 928.
- 3 Y. Y. Lu, Z. Y. Tu and L. A. Archer, *Nat. Mater.*, 2014, **13**, 961.
- 4 D. C. Lin, Y. Y. Liu and Y. Cui, *Nat. Nanotechnol.*, 2017, **12**, 194.
- 5 S. Choudhury and L. A. Archer, *Adv. Electron. Mater.*, 2016, **2**, 1500246.
- 6 J. Zhao, L. Liao, F. F. Shi, T. Lei, G. X. Chen, A. Pei, J. Sun, K. Yan, G. M. Zhou, Z. N. Bao and Y. Cui, *J. Am. Chem. Soc.*, 2017, **139**, 33.
- 7 W. Xu, J. L. Wang, F. Ding, X. L. Chen, E. Nasybulin, Y. Zhang and J. G. Zhang, *Energy Environ. Sci.*, 2014, **7**, 513.
- 8 X. B. Cheng, R. Zhang, C. Z. Zhao, F. Wei, J. G. Zhang and Q. Zhang, *Adv. Sci.*, 2016, **3**, 1500213.
- 9 Y. Y. Liu, D. C. Lin, Y. Z. Li, G. X. Chen, A. Pei, O. Nix, Y. B. Li and Y. Cui, *Nat. Commun.*, 2018, **9**, 3656.
- 10 X. Li, J. M. Zheng, X. D. Ren, M. H. Engelhard, W. T. Zhao, Q. Y. Li, J. G. Zhang and W. Xu, *Adv. Energy Mater.*, 2018, **8**, 1703022.
- 11 D. C. Lin, Y. Y. Liu, W. Chen, G. M. Zhou, K. Liu, B. Dunn and Y. Cui, *Nano Lett.*, 2017, **17**, 6.
- 12 Q. Zhao, Z. Y. Tu, S. Y. Wei, K. H. Zhang, S. Choudhury, X. T. Liu and L. A. Archer, *Angew. Chem.*, 2018, **130**, 1004.
- 13 K. J. Harry, D. T. Hallinan, D. Y. Parkinson, A. A. Macdowell and N. P. Balsara, *Nat. Mater.*, 2014, **13**, 69.
- 14 S. Chandrashekar, N. M. Trease, H. J. Chang, L. S. Du, C. P. Grey and A. Jerschow, *Nat. Mater.*, 2012, **11**, 311.
- 15 R. Bhattacharyya, B. Key, H. Chen, A. S. Best, A. F. Hollenkamp and C. P. Grey, *Nat. Mater.*, 2010, **9**, 504.
- 16 D. C. Lin, Y. Y. Liu, Z. Liang, H. Lee, J. Sun, H. T. Wang, K. Yan, J. Xie and Y. Cui, *Nat. Nanotechnol.*, 2016, **11**, 626.
- 17 G. Y. Zheng, S. W. Lee, Z. Liang, H. W. Lee, K. Yan, H. B. Yao, H. T. Wang, W. Y. Li, S. Chu and Y. Cui, *Nat. Nanotechnol.*, 2014, **9**, 618.
- 18 A. C. Kozen, C. F. Lin, A. J. Pearse, M. A. Schroeder, X. G. Han, L. B. Hu, S. B. Lee, G. W. Rubloff and M. Noked, *ACS Nano*, 2015, **9**, 6.
- 19 S. Choudhury, Z. Y. Tu, S. Stalin, D. Vu, K. Fawole, D. Gunceler, R. Sundararaman and L. A. Archer, *Angew. Chem.*, 2017, **56**, 13070.
- 20 C. Yan, Y. X. Yao, X. Chen, X. B. Cheng, X. Q. Zhang, J. Q. Huang and Q. Zhang, *Angew. Chem.*, 2018, **130**, 1.
- 21 C. Yan, X. B. Cheng, Y. X. Yao, X. Shen, B. Q. Li, W. J. Li, R. Zhang, J. Q. Huang, H. Li and Q. Zhang, *Adv. Mater.*, 2018, **180**, 4461.
- 22 K. Yan, H. W. Lee, T. Gao, G. Y. Zheng, H. B. Yao, H. T. Wang, Z. D. Lu, Y. Zhou, Z. Liang, Z. F. Liu, S. Chu and Y. Cui, *Nano Lett.*, 2014, **14**, 10.
- 23 E. Kazyak, K. N. Wood and N. P. Dasgupta, *Chem. Mater.*, 2015, **27**, 18.
- 24 M. D. Tikekar, S. Choudhury, Z. Tu and L. A. Archer, *Nat. Energy*, 2016, **1**, 16114.

- 25 X. Cheng, R. Zhang, C. Zhao, F. Wei, J. Zhang and Q. Zhang, *Adv. Sci.*, 2016, **3**, 1.
- 26 Z. Tu, P. Nath, Y. Lu, M. D. Tikekar and L. A. Archer, *Acc. Chem. Res.*, 2015, **48**, 2947.
- 27 Q. Zhao, X. T. Liu, S. J. Stalin, K. Khan and L. A. Archer, *Nat. Energy*, 2019, **4**, 365.
- 28 S. H. Jiao, X. D. Ren, R. G. Cao, M. H. Engelhard, Y. Z. Liu, D. H. Hu, D. G. Mei, J. M. Zheng, W. G. Zhao, Q. Y. Li, N. Liu, B. D. Adams, C. Ma, J. Liu, Z. G. Zhang and W. Xu, *Nat. Energy*, 2018, **3**, 739.
- 29 R. Pathak, K. Chen, A. Gurung, K. M. Reza, B. Bahrami, F. Wu, A. Chaudhary, N. Ghimire, B. Zhou, W. H. Zhang, Y. Zhou and Q. Q. Qiao, *Adv. Energy Mater.*, 2019, **9**, 1901486.
- 30 X. Liang, Q. Pang, I. R. Kochetkov, M. S. Sepere, H. huang, X. Q. Sun and L. F. Nazar, *Nat. Energy*, 2017, **7**, 31.
- 31 X. S. Wang, X. L. Liao, W. N. Huang, L. D. Xing, Y. H. Liao, Q. M. Huang, M. Q. Xu and W. S. Li, *Electrochim. Acta*, 2015, **184**, 94.
- 32 L. N. Wang, A. Menakath, F. D. Han, Y. Wang, P. Y. Zavalij, K. J. Gaskell, O. Borodin, D. Luga, S. P. Brown, C. S. Wang, K. Xu and B. W. Eichhorn, *Nat. Chem.*, 2019, **11**, 789.
- 33 Z. S. Wang, M. M. Rao, J. H. Li, C. C. Ye, Z. D. Liu, Q. S. Xu, X. J. Jin, R. A. Du, Q. M. Xie, W. Luo, W. S. Li and Y. C. Qiu, *J. Electroanal. Chem.*, 2019, **851**, 113411.
- 34 X. Li, J. Zheng, X. D. Ren, M. H. Engelhard, W. G. Zhao, Q. Y. Li, J. G. Zhang and W. Xu, *Adv. Energy Mater.*, 2018, **8**, 1703022.
- 35 C. Yan, X. B. Cheng, Y. Tian, X. Chen, X. Q. Zhang, W. J. Li, J. W. Huang and Q. Zhang, *Adv. Mater.*, 2018, **30**, 1707629.
- 36 W. Kohn and L. J. Sham, *Phys. Rev.*, 1965, **140**, A1133.
- 37 S. L. Dudarev, G. A. Botton, S. Y. Savrasov, C. J. Humphreys and A. P. Sutton, *Phys. Rev.*, 1998, **57**, 1505.
- 38 H. J. Monkhorst and J. D. Pack, *Phys. Rev.*, 1976, **13**, 5188.
- 39 H. Graeme, B. P. Uberuaga and J. Hannes, *J. Chem. Phys.*, 2000, **113**, 9901.
- 40 Z. M. Xu, J. Chen, L. X. Jiang, Y. Q. Lai and J. Li, *Phys. Chem. Chem. Phys.*, 2017, **19**, 7807.
- 41 D. Rao, L. Zhang, Z. Meng, Y. Wang, G. Qiao, X. Shen, H. Xia, J. Liu and R. Lu, *J. Mater. Chem. A*, 2017, **5**, 2328.
- 42 B. D. Adams, J. M. Zheng, X. D. Ren, W. Xu and J. G. Zhang, *Adv. Energy Mater.*, 2017, **8**, 1702097.